IIETA International Information and Engineering Technology Association
Advancing the World of Information and Engineering

Mathematical Modelling of Engineering Problems
Vol. 13, No. 1, January, 2026, pp. 111-118
Journal homepage: http://iieta.org/journals/mmep

A Homography-Based Planar Coordinate Calibration Method for Machine Vision Systems

Ngoc-Vu Ngo

Faculty of Mechanical Engineering, Thai Nguyen University of Technology (TNUT), Thai Nguyen 250000, Vietnam

Corresponding Author Email: ngocvu@tnut.edu.vn

https://doi.org/10.18280/mmep.130111

Received: 6 November 2025
Revised: 16 January 2026
Accepted: 24 January 2026
Available online: 28 February 2026

Keywords:
machine vision, planar calibration, homography estimation, reprojection error, coordinate transformation, robot manipulation

ABSTRACT

Coordinate calibration is a fundamental process in machine vision systems, as it directly affects the measurement accuracy and efficiency of the system. In this study, an experimental model for planar coordinate calibration using a homography transformation was developed. A two-dimensional calibration board comprising 140 black circles with a diameter of 10 mm was designed to generate the world coordinates. The corresponding image coordinates were acquired using a complementary metal-oxide semiconductor camera mounted above the calibration board. The captured images were processed using image processing and machine vision software to extract the coordinates of the circle centers. Subsequently, the world coordinates and the corresponding image coordinates were used to compute the homography matrix. Using this matrix, the reprojection image coordinates were obtained, and the reprojection error of each calibration point, as well as the average reprojection error of all 140 calibration points, were calculated and evaluated. The experimental results indicate that the average reprojection error was 0.677 pixels. Additionally, the coordinate calibration error for most calibration points ranged from −0.6 mm to 0.5 mm along the *OX* axis and from −0.6 mm to 0.6 mm along the *OY* axis. The proposed method was further validated to determine the real-world positions of objects for robot manipulation.

1. INTRODUCTION

In recent years, along with the rapid development of science and technology, the Fourth Industrial Revolution and artificial intelligence (AI) have given rise to many advanced technologies that have strongly impacted production and daily life. Among these, machine vision technology has emerged as a key innovation. The operating principle of this technology is similar to that of the human eye: it uses cameras to capture image data, which is then processed using image processing and machine vision software to identify the characteristics of objects of interest, such as shape, color, size, or position. Typically, a machine vision system consists of one or more cameras connected to a computer, along with a light source to assist the camera during image acquisition.

Currently, machine vision technology is applied in many fields, including product quality inspection, automated optical inspection (AOI) systems [1, 2], industrial automation lines [3], semiconductor and electronics manufacturing [4, 5], medical image analysis [6, 7], defect detection [8, 9], and non-contact measurement applications [10-12].

In machine vision systems, coordinate calibration is to establish the mapping between image coordinates and their corresponding world coordinates. To date, many studies have focused on developing algorithms and calibration methods to enhance the accuracy and efficiency of machine vision systems. For instance, Lee et al. [13] introduced a camera calibration technique using a line classification method. This technique relied on an end-to-end neural network designed for single-image camera calibration to directly estimate the intrinsic and extrinsic camera parameters from an image and a corresponding family of line segments. To further improve learning efficiency, an auxiliary line classification work, allowing the network to effectively capture and encode global geometric information from linear features, was investigated. The reported findings indicated that this technique achieved state-of-the-art performance. Nguyen et al. [14] presented an unsupervised learning framework to train a deep convolutional neural network for estimating planar homographies. Experimental evaluations demonstrated that their algorithm achieved faster inference speed while maintaining comparable, and in some cases superior, levels of accuracy and robustness under varying lighting conditions. In related work by Wang et al. [15], a new homography estimation technique based on a self-supervised regression network was investigated. In this study, spatial pyramid pooling modules were employed to improve feature extraction quality by using contextual information from multiple receptive fields within each image. Experiments on the synthetic dataset revealed that the proposed technique outperformed several existing approaches. Fang et al. [16] investigated a learning-based algorithm for regressing per-sequence calibration parameters based on an efficient family of generalized camera models. The proposed method achieved self-calibration results with sub-pixel reprojection error. Furthermore, their method was validated across diverse camera properties, including

perspective, fisheye, and catadioptric configurations. Experimental findings indicated that their approach effectively improved depth estimation for machine vision systems. In another study, Lee et al. [17] presented a neural scene parser for single-image camera calibration in man-made environments. Their approach exploited semantic and geometric cues, resulting in substantial gains in calibration accuracy. The proposed structure comprised two networks. The first estimated the zenith vanishing point and generated multiple candidates defined by the rotation and focal length of the camera, while the second one evaluated each candidate using the input image and the geometric cues. The study demonstrated that this technique outperformed conventional single-image camera calibration techniques in both indoor and outdoor scenarios.

In addition, Schaffalitzky and Zisserman [18] described the geometry of three different structures, including a set of equally spaced coplanar parallel lines, a planar pattern generated through translational repetition of a fundamental element, and a collection of elements organized in a regular planar grid. Their method indicated that the output produced by geometric grouping algorithms can be exploited for unsupervised vanishing point estimation and line detection. Le et al. [19] trained neural networks using only image pairs. The images were aligned through homography mapping. They investigated and discussed how to make and train a deep neural network capable of handling dynamic environments. Experimental findings demonstrated that their method could robustly estimate homographies in complex scenarios involving dynamic environments, blurred images, or a shortage of textures. In another study, Yu et al. [20] presented a technique for improving camera calibration accuracy using a high-precision calibration board. In this method, regularly distributed target markers in the form of concentric ring patterns were displayed on a liquid crystal display (LCD) panel. Sub-pixel edges were then located at multiple positions on the liquid crystal display panel. These sub-pixel edge points were then transformed into parameter space to make a family of lines, and the intersections of these lines were regarded as the center pixel coordinates of the calibration targets. Experimental findings demonstrated that their method was practical and straightforward to implement. Su et al. [21] proposed a technique for recovering the intrinsic parameters of cameras using two views of a planar surface. This study introduced new homography-mapping-based minimal solutions for camera self-calibration. Specifically, 2.5-point and 3.5-point camera self-calibration algorithms for points on the ground plane were utilized to enable simultaneous estimation of the camera focal length and principal point. This study demonstrated the practicality and efficiency of these algorithms in terms of reliability under various noise levels and different camera configurations. Zhang et al. [22] presented a novel method for estimating the six-degree-of-freedom camera extrinsic parameters in a robot vision system. In this method, homography mapping between the plane images of two cameras was used. A closed-form solution for the rotation matrix and the translation vector of the camera extrinsic parameters was derived from the characteristics of the eigenvalues and eigenvectors. The experimental findings demonstrated that their method was effective and achieved satisfactory performance.

Furthermore, homography-based coordinate calibration has been successfully applied to robotic manipulation and high-precision planar measurement systems. Ngo and Van [23] developed a vision-based automatic classification system for mechanical and measurement components handled by robot arms. In this study, the authors introduced an algorithm for coordinate calibration process. Experimental data were used to transform coordinates from the image plane to the world coordinate system, enabling accurate determination of object positions. The calibrated coordinate data were then transmitted to the robot for automated classification. This proposed system is simple, efficient, and user-friendly. Wang et al. [24] introduced a perspective distortion compensation technique for planar imaging to improve pixel-level equivalence and measurement accuracy in machine vision systems**.** In their study, a rectified image plane was constructed and calibrated through homography mappings among the measurement plane, the original image plane, and the rectified plane**.** Parameters, including radius, length, angle, and area of a designed pattern, were evaluated during the investigation process**.** The experimental findings indicated that the proposed approach achieved reliable high-precision planar measurements even in the presence of perspective distortion.

Previous studies have shown that a considerable number of studies have concentrated on coordinate and camera calibration processes for machine vision systems utilized in various applications, yielding substantial benefits. However, existing calibration approaches still face several challenges. Therefore, it remains necessary to continue conducting research and developing experimental models for these processes in machine vision systems using homography transformations, and to evaluate the reprojection accuracy of the proposed method.

2. METHODOLOGY

2.1 Perspective transformation

Perspective transformation refers to the projection of a point from real space (3-D) onto the image plane (2-D), as illustrated in Figure 1. In this model, *oxyz* represents the camera coordinate system. The image plane coincides with both the *xoy* and *XOY* planes. The optical axis passes through the center of the lens and lies along the *z*- and *Z*-axes of the two coordinate systems. Therefore, the center of the image plane is placed at the origin, and the coordinates of the lens center are $(0, 0, \lambda)$, where λ denotes the focal length.

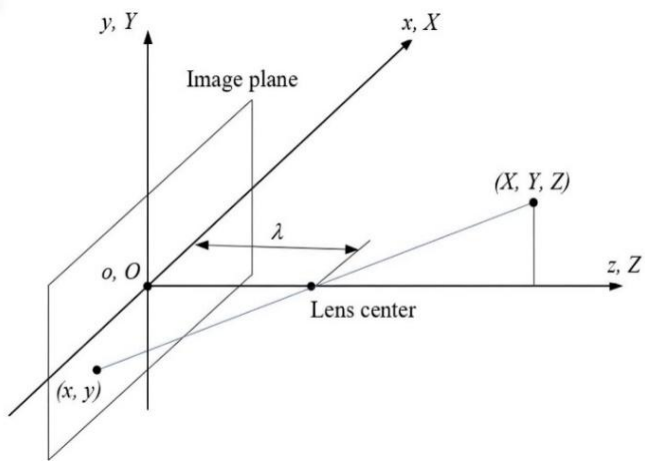

Figure 1. Perspective transformation model

Supposing that the camera coordinate system *oxyz* coincides with the world coordinate system *OXYZ*, and that $Z > \lambda$ (all measured points are in front of the lens), the mapping between the image coordinates (x, y) and the world coordinates (X, Y, Z) can be derived using similar triangles in the *xoz* and *yoz* planes, respectively.

In this method, the inverse perspective transformation enables the determination of a point in real space with coordinates (X, Y, Z) from an image point with coordinates (x, y), as expressed in Eq. (1):

$$w_h = P^{-1} c_h \tag{1}$$

where, P denotes the perspective projection matrix.

2.2 Determination of the homography matrix

Within the framework of the camera model [25], both intrinsic and extrinsic parameters are, in principle, directly measurable. However, when the camera is employed as a quantitative measurement device, accurately determining one or more of these parameters often becomes complex in practice. This estimation process necessitates a collection of image pixels that correspond to predefined world coordinates serving as reference points. The systematic procedure of computing the camera model parameters from these known spatial references is commonly defined as camera calibration, which establishes the mathematical mapping between the image plane and the world coordinate system.

According to the camera model, we have:

$$c_h = A w_h \tag{2}$$

where, $\boldsymbol{c_h}$ represents the camera coordinate matrix, $\boldsymbol{A}$ represents the homography matrix, and $\boldsymbol{w_h}$ represents the world coordinate matrix.

In 2-D space, Eq. (2) can be described in the following homogeneous form:

$$\begin{bmatrix} sx \\ sy \\ s \end{bmatrix} = \begin{bmatrix} a_{11} & a_{12} & a_{13} \\ a_{21} & a_{22} & a_{23} \\ a_{31} & a_{32} & a_{33} \end{bmatrix} \begin{bmatrix} X \\ Y \\ 1 \end{bmatrix} \tag{3}$$

where, s denotes the scaling factor, and $s \neq 0$. By replacing $sx = x \cdot s$ and $sy = y \cdot s$ into the matrix equation and expanding it, Eq. (4) is obtained as follows:

$$\begin{cases} Xa_{11} + Ya_{12} + 1a_{13} + 0a_{21} + 0a_{22} + 0a_{23} - xXa_{31} - xYa_{32} - xa_{33} = 0 \\ 0a_{11} + 0a_{12} + 0a_{13} + Xa_{21} + Ya_{22} + 1a_{23} - yXa_{31} - yYa_{32} - ya_{33} = 0 \end{cases} \tag{4}$$

Eq. (4) contain eight unknowns. To determine these unknowns in matrix $\boldsymbol{A}$, the world coordinates (X_i, Y_i) of at least four points and their corresponding image coordinates (x_i, y_i) are substituted into Eq. (4). Consequently, Eq. (5) can be expressed as follows:

$$\begin{bmatrix} X_1 & Y_1 & 1 & 0 & 0 & 0 & -x_1X_1 & -x_1Y_1 & -x_1 \\ 0 & 0 & 0 & X_1 & Y_1 & 1 & -y_1X_1 & -y_1Y_1 & -y_1 \\ X_2 & Y_2 & 1 & 0 & 0 & 0 & -x_2X_2 & -x_2Y_2 & -x_2 \\ 0 & 0 & 0 & X_2 & Y_2 & 1 & -y_2X_2 & -y_2Y_2 & -y_2 \\ X_3 & Y_3 & 1 & 0 & 0 & 0 & -x_3X_3 & -x_3Y_3 & -x_3 \\ 0 & 0 & 0 & X_3 & Y_3 & 1 & -y_3X_3 & -y_3Y_3 & -y_3 \\ X_4 & Y_4 & 1 & 0 & 0 & 0 & -x_4X_4 & -x_4Y_4 & -x_4 \\ 0 & 0 & 0 & X_4 & Y_4 & 1 & -y_4X_4 & -y_4Y_4 & -y_4 \end{bmatrix} \begin{bmatrix} a_{11} \\ a_{12} \\ a_{13} \\ a_{21} \\ a_{22} \\ a_{23} \\ a_{31} \\ a_{32} \end{bmatrix} = \begin{bmatrix} 0 \\ 0 \\ 0 \\ 0 \\ 0 \\ 0 \\ 0 \\ 0 \end{bmatrix} \tag{5}$$

Since the homography matrix $\boldsymbol{A}$ is defined up to a scale factor s, one element in Eq. (5) can be arbitrarily fixed to resolve this scale ambiguity. In this study, a_{33} is set to 1, resulting in eight independent unknown parameters in matrix $\boldsymbol{A}$.

3. EXPERIMENTAL MODEL

3.1 Experimental system

The experimental system, as shown in Figure 2, consists of a calibration board, a CMOS camera, a light source positioned beneath the calibration board, and a computer fitted with image processing and machine vision software. The CMOS camera was utilized to capture the image data. This camera was rigidly mounted above the calibration board to ensure mechanical stability and was carefully adjusted to achieve optimal focus prior to image acquisition. The detailed technical specifications of the camera are presented in Table 1.

3.2 Calibration board

To obtain the world coordinates, a 2-D calibration board was developed, as shown in Figure 3. It included 140 black circles, each with a diameter of 10 mm. The centers of the circles were spaced 20 mm apart along both the X- and Y-axes. The corresponding world coordinates (X, Y) of the calibration points are summarized in Table 2.

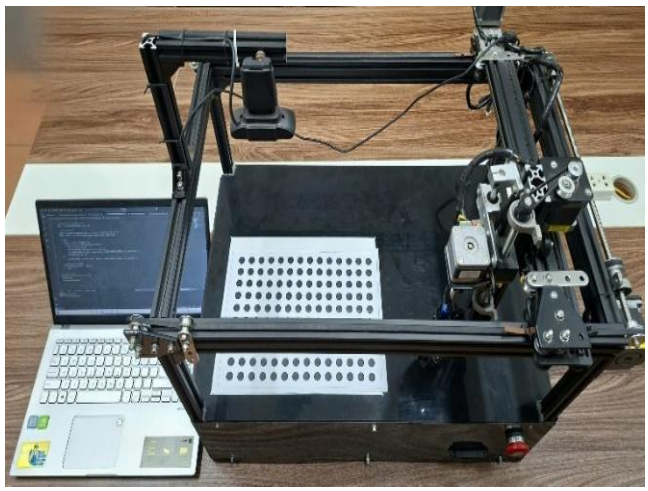

Figure 2. Experimental system

Table 1. Camera specifications

No.	Specifications
1	High-Definition (HD) video calling (1280 × 720 pixels)
2	HD video recording: Up to 1280 × 720 pixels
3	Logitech Fluid Crystal™ technology
4	Autofocus
5	Photo: Up to 8 megapixels
6	High-speed Universal Serial Bus (USB) 2.0 port
7	Lens and sensor type: Plastic

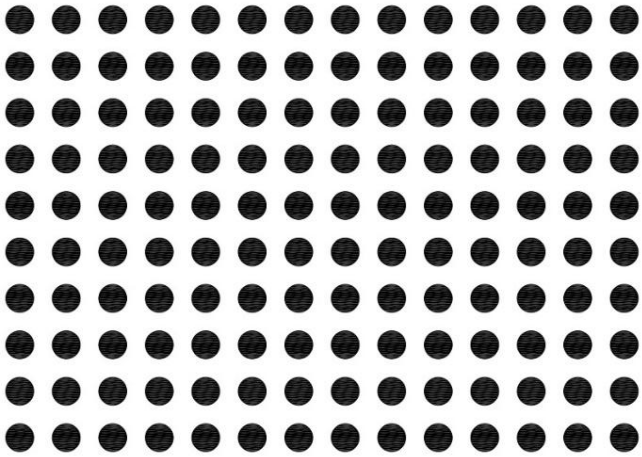

Figure 3. Calibration board

Table 2. World and image coordinates of calibration points

Points	Original World Coordinates (mm)			Original Image Coordinates (Pixels)	
	X	*Y*	*Z*	*x*	*y*
1	0	0	0	195	143
2	20	0	0	233	143
3	40	0	0	271	144
4	60	0	0	309	144
5	80	0	0	347	145
6	100	0	0	384	145
7	120	0	0	422	145
8	140	0	0	460	145
9	160	0	0	497	145
10	180	0	0	535	145
11	200	0	0	573	145
12	220	0	0	611	145
13	240	0	0	650	145
14	260	0	0	688	144
…	…	…	…	…	…
127	0	180	0	188	482
128	20	180	0	227	482
129	40	180	0	266	482
130	60	180	0	304	482
131	80	180	0	342	483
132	100	180	0	381	483
133	120	180	0	419	483
134	140	180	0	457	483
135	160	180	0	495	483
136	180	180	0	533	484
137	200	180	0	572	484
138	220	180	0	610	485
139	240	180	0	649	485
140	260	180		688	486

3.3 Determination of the image coordinates

In this section, to identify the corresponding image coordinates, the image data captured by the camera was transmitted to a computer equipped with image processing and machine vision software. The software detected the black circles on the calibration board image using a circle grid detection algorithm, thereby determining the center coordinates of these circles, as shown in Figure 4. The corresponding image coordinates (x, y) of the circle centers are summarized in Table 2.

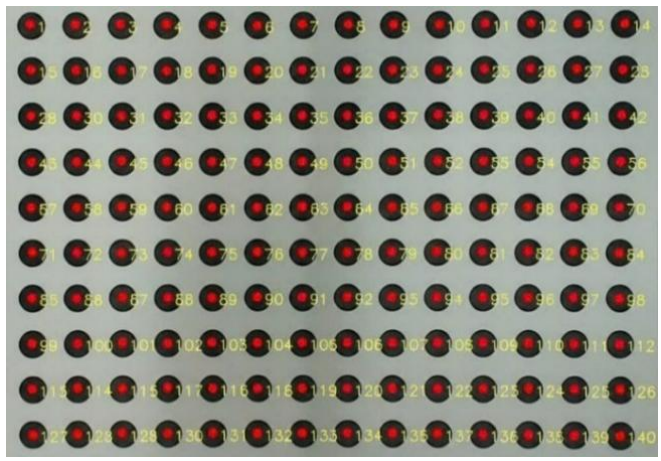

Figure 4. Recognition results

4. RESULTS AND DISCUSSIONS

4.1 Homography matrix *A*

By substituting the world coordinates of 140 calibration points and their corresponding image coordinates into Eq. (6), the coefficients a_{11}, a_{12}, a_{13}, a_{21}, a_{22}, a_{23}, a_{31}, a_{32}, with $a_{33} = 1$, are determined. The homography matrix $\boldsymbol{A}$ is then expressed in the following form:

$$A = \begin{bmatrix} 1.878 & 0.043 & 195.671 \\ 0.003 & 1.851 & 144.233 \\ 0.00002 & 0.00006 & 1.0000 \end{bmatrix}$$

4.2 Reprojection image coordinates

Once the homography matrix $\boldsymbol{A}$ is determined, the reprojection accuracy can be evaluated by calculating the reprojection image coordinates as follows:

$$c_h = \begin{bmatrix} 1.878 & 0.043 & 195.671 \\ 0.003 & 1.851 & 144.233 \\ 0.00002 & 0.00006 & 1.0000 \end{bmatrix} w_h$$

The reprojection image coordinates are summarized in Table 3.

4.3 Reprojection error

4.3.1 Reprojection error of each calibration point

To investigate the reprojection accuracy, the pixel reprojection error is computed using the following Eq. (6):

$$e_i = \sqrt{(x_i - x_{ci})^2 + (y_i - y_{ci})^2} \quad (6)$$

where, e_i denotes the reprojection error of each calibration point; x_i and y_i denote the coordinates of the original image pixels; x_{ci} and y_{ci} denote the coordinates of the reprojected

pixels obtained from the homography matrix $\boldsymbol{A}$, corresponding to the x- and y-axes, respectively. Here, i denotes the index of the calibration points. The calculated pixel reprojection errors are shown in Table 3.

4.3.2 Average reprojection error

The average reprojection error of all calibration points is determined by Eq. (7), as follows:

$$\Delta = \frac{1}{N}\sum_{i=1}^{N} e_i \tag{7}$$

where, Δ denotes the average reprojection error of the calibration points. N represents the number of the calibration points. Then, the average error is:

$$\Delta = \frac{1.400 + 1.378 + \cdots + 0.130 + 0.783 + 1.484}{140} = 0.677(pixels)$$

From Table 3, it can be observed that the maximum pixel reprojection error is 1.911 pixels, while the minimum is 0.014 pixels. The average reprojection error calculated from the 140 calibration points is 0.677 pixels. This level of error is acceptable and demonstrates that the proposed technique can be effectively applied in machine vision systems for robot navigation and object localization in 3D space.

4.3.3 Calibration results

Once the homography matrix $\boldsymbol{A}$ is determined, the world coordinates corresponding to the image data will be computed using Eq. (8), as follows:

$$w_h = A^{-1}c_h \tag{8}$$

where, $\boldsymbol{A}^{-1}$ denotes the inverse matrix of the homography matrix $\boldsymbol{A}$. The world coordinate data are shown in Table 4.

4.3.4 Calibration deviation

The error analysis results from Table 4 are illustrated in Figure 5. The deviations along the OX axis remain relatively stable, mostly ranging from −0.6 mm to 0.5 mm. Similarly, the deviations along the OY axis are also stable, varying mainly from −0.8 mm to 0.6 mm. The maximum negative deviations are −0.859 mm at point 113 and −0.913 mm at point 14 along the X- and Y-axes, respectively. Conversely, the maximum positive deviations are 0.460 mm at point 47 and 0.576 mm at point 64 along the X- and Y-axes, respectively. The relatively large deviations observed at points 14 and 113 may be caused by external factors such as lighting conditions, image processing algorithms, or noise during image acquisition. However, these deviations have a negligible influence on the calibration process and do not significantly affect the overall accuracy of the system.

Table 3. Reprojection error of each calibration point (pixel)

Points	Original Image Coordinates		Reprojected Image Coordinates		Reprojection Errors
	x	y	x_c	y_c	e
1	195	143	195.67	144.23	1.400
2	233	143	233.32	144.34	1.378
3	271	144	271	144.45	0.450
4	309	144	308.7	144.56	0.635
5	347	145	346.44	144.67	0.650
6	384	145	384.2	144.78	0.297
7	422	145	421.99	144.89	0.110
8	460	145	459.82	145.01	0.180
9	497	145	497.67	145.12	0.681
10	535	145	535.55	145.23	0.596
11	573	145	573.45	145.34	0.564
12	611	145	611.39	145.45	0.595
13	650	145	649.36	145.56	0.850
14	688	144	687.35	145.67	1.792
…	…	…	…	…	
127	188	482	189.89	482.28	1.911
128	227	482	227.92	482.52	1.057
129	266	482	265.98	482.76	0.760
130	304	482	304.08	483.01	1.013
131	342	483	342.2	483.25	0.320
132	381	483	380.35	483.49	0.814
133	419	483	418.53	483.73	0.868
134	457	483	456.74	483.97	1.004
135	495	483	494.98	484.22	1.220
136	533	484	533.25	484.46	0.524
137	572	484	571.55	484.7	0.832
138	610	485	609.88	484.95	0.130
139	649	485	648.24	485.19	0.783
140	688	486	686.63	485.43	1.484

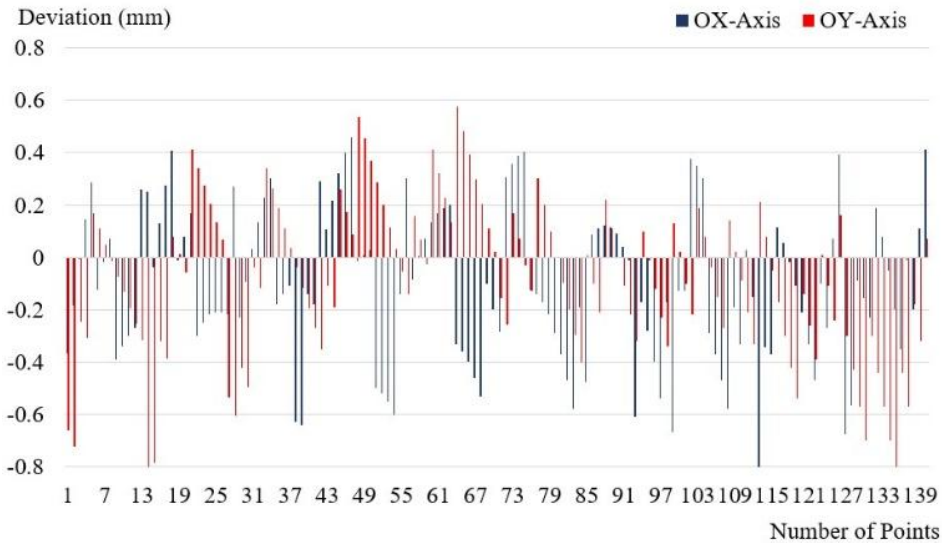

Figure 5. Calibration deviation diagram

Table 4. World coordinate data and calibration deviation (mm)

Points	Original World Coordinates			World Coordinates After Calibration		Calibration Deviation	
	X	*Y*	*Z*	*X*	*Y*	*ΔX*	*ΔY*
1	0	0	0	-0.367	-0.662	-0.367	-0.662
2	20	0	0	19.817	-0.723	-0.183	-0.723
3	40	0	0	39.993	-0.246	-0.007	-0.246
4	60	0	0	60.144	-0.307	0.144	-0.307
5	80	0	0	80.286	0.169	0.286	0.169
6	100	0	0	99.876	0.109	-0.124	0.109
7	120	0	0	119.980	0.048	-0.02	0.048
8	140	0	0	140.07	-0.013	0.07	-0.013
9	160	0	0	159.61	-0.072	-0.39	-0.072
10	180	0	0	179.66	-0.133	-0.34	-0.133
11	200	0	0	199.7	-0.194	-0.3	-0.194
12	220	0	0	219.73	-0.255	-0.27	-0.255
13	240	0	0	240.26	-0.317	0.26	-0.317
14	260	0	0	260.25	-0.913	0.25	-0.913
…	…	…	…	…	…	…	…
127	0	180	0	-0.677	179.7	-0.677	-0.3
128	20	180	0	19.434	179.57	-0.566	-0.43
129	40	180	0	39.909	179.43	-0.091	-0.57
130	60	180	0	59.844	179.3	-0.156	-0.7
131	80	180	0	79.768	179.7	-0.232	-0.3
132	100	180	0	100.19	179.56	0.19	-0.44
133	120	180	0	120.08	179.43	0.08	-0.57
134	140	180	0	139.95	179.3	-0.05	-0.7
135	160	180	0	159.8	179.17	-0.2	-0.83
136	180	180	0	179.65	179.56	-0.35	-0.44
137	200	180	0	199.99	179.43	-0.01	-0.57
138	220	180	0	219.8	179.82	-0.2	-0.18
139	240	180	0	240.11	179.68	0.11	-0.32
140	260	180	0	260.41	180.07	0.41	0.07

4.4 Determination of the object position

In order to locate the shape and position of objects in the robot's working area, this study applied image processing algorithms. First, to simplify the data obtained from the camera, the color image was converted to a grayscale image according to Eq. (9), as follows:

$$Gray = 0.299R + 0.587G + 0.114B \quad (9)$$

where, *R*, *G,* and *B* denote the primary color channels red, green, and blue, respectively.

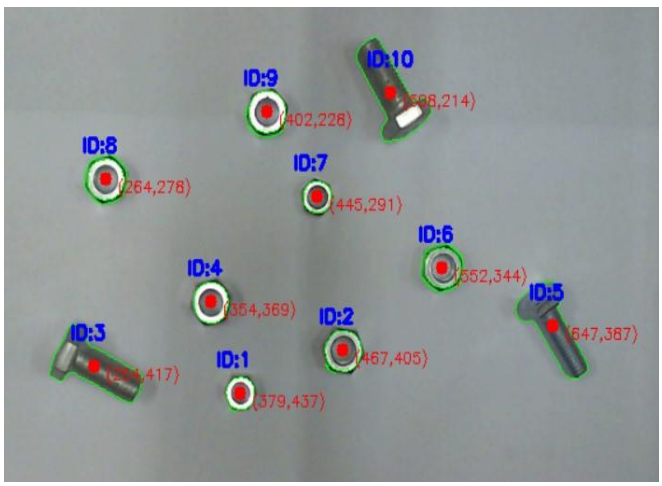

Figure 6. Determination of object positions in the world coordinate system

In the next step, the Gaussian blur algorithm was applied to reduce image noise and smooth the image, thereby facilitating subsequent processing steps. The Canny edge detection algorithm was then utilized to detect object edges in regions with abrupt changes in light intensity. Finally, the contour-finding algorithm was used to trace and determine the contours of the objects, completing the recognition process.

To accurately determine the position of each object in the image, the centroid coordinates (*cx*, *cy*) were calculated using image moments. The corresponding image coordinates and identification codes (IDs) of the objects were then displayed directly on the processed image, as illustrated in Figure 6.

The calibration results have been applied to estimate the positions of objects in the workspace of a robot arm. The world coordinates of the objects are presented in Table 5.

Table 5. Coordinate data of objects

Objects	Image Coordinates (Pixel)		World Coordinates (mm)	
	x	*y*	*X*	*Y*
ID:1	379	437	98.894	155.901
ID:2	467	405	144.330	138.238
ID:3	254	417	33.108	145.221
ID:4	354	369	85.371	120.079
ID:5	647	387	238.437	128.740
ID:6	552	344	189.182	106.304
ID:7	445	291	132.812	78.483
ID:8	264	278	37.317	71.999
ID:9	402	228	109.847	45.032
ID:10	508	214	165.662	37.346

Note: ID: identification code

5. CONCLUSIONS

In this study, an experimental model was developed to determine the homography matrix $\boldsymbol{A}$ in planar coordinate calibration for machine vision systems. The proposed system included a fixed Logitech C525 camera and a 2-D calibration board consisting of 140 calibration points. The image coordinates were obtained using image analysis and processing. Both the image coordinates and the world coordinates were then used to determine the homography matrix $\boldsymbol{A}$, establishing the relationship between the two coordinate systems. The accuracy of the calibration process was evaluated by calculating the reprojection error of each image point and the average error of all image points. Furthermore, calibration deviations were analyzed to validate the consistency of the results. This method was applied to calculate the world coordinates of objects within a robot arm's workspace, including three bolts and seven nuts. The experimental results demonstrate that the proposed method is effective and suitable for the planar coordinate calibration process for machine vision systems used for object localization in industrial robots in 2-D space. For future work, to further enhance calibration accuracy and reduce noise, higher-resolution cameras and optimized lighting conditions under controlled environments will be investigated.

ACKNOWLEDGMENT

The study was supported by Thai Nguyen University of Technology (TNUT), Thai Nguyen, Vietnam.

REFERENCES

[1] Xiang, R., He, W., Zhang, X., Wang, D., Shan, Y. (2018). Size measurement based on a two-camera machine vision system for the bayonets of automobile brake pads. Measurement, 122: 106-116. https://doi.org/10.1016/j.measurement.2018.03.017

[2] Balasundaram, M.K., Ratnam, M.M. (2014). In-process measurement of surface roughness using machine vision with sub-pixel edge detection in finish turning. International Journal of Precision Engineering and Manufacturing, 15(11): 2239-2249. https://doi.org/10.1007/s12541-014-0587-3

[3] Mishra, A., Sainul, I.A., Bhuyan, S., Deb, S., Sen, D., Deb, A.K. (2018). Development of a flexible assembly system using industrial robot with machine vision guidance and dexterous multi-finger gripper. In Precision Product-Process Design and Optimization, pp. 31-71. https://doi.org/10.1007/978-981-10-8767-7_2

[4] Huang, S.H., Pan, Y.C. (2015). Automated visual inspection in the semiconductor industry: A survey. Computers in Industry, 66: 1-10. https://doi.org/10.1016/j.compind.2014.10.006

[5] Silva, C.A.D.S., Paladini, E.P. (2025). Smart machine vision system to improve decision-making on the assembly line. Machines, 13(2): 98. https://doi.org/10.3390/machines13020098

[6] Najrabi, D., Hamghalam, M., Ayatollahi, A. (2018). Diagnosis of astrocytoma and globalastom using machine vision. In 2018 6th Iranian Joint Congress on Fuzzy and Intelligent Systems (CFIS), Kerman, Iran, pp. 152-155. https://doi.org/10.1109/CFIS.2018.8336661

[7] Možina, M., Tomaževič, D., Pernuš, F., Likar, B. (2013). Automated visual inspection of imprint quality of pharmaceutical tablets. Machine Vision and Applications, 24(1): 63-73. https://doi.org/10.1007/s00138-011-0366-4

[8] Chauhan, V., Surgenor, B. (2017). Fault detection and classification in automated assembly machines using machine vision. The International Journal of Advanced Manufacturing Technology, 90(9-12): 2491-2512. https://doi.org/10.1007/s00170-016-9581-5

[9] Kumar, G.S., Natarajan, U., Ananthan, S.S. (2012). Vision inspection system for the identification and classification of defects in MIG welding joints. The International Journal of Advanced Manufacturing Technology, 61(9-12): 923-933. https://doi.org/10.1007/s00170-011-3770-z

[10] Ngo, N.V., Hsu, Q.C., Hsiao, W.L., Yang, C.J. (2017). Development of a simple three-dimensional machine-vision measurement system for in-process mechanical parts. Advances in Mechanical Engineering, 9(10): 1-11. https://doi.org/10.1177/1687814017717183

[11] Ali, M.H., Kurokawa, S., Uesugi, K. (2014). Camera based precision measurement in improving measurement accuracy. Measurement, 49: 138-147. https://doi.org/10.1016/j.measurement.2013.11.057

[12] Rejc, J., Kovačič, F., Trpin, A., Turk, I., Štrus, M., Rejc, D., Munih, M. (2011). The mechanical assembly dimensional measurements with the automated visual inspection system. Expert Systems with Applications, 38(8): 10665-10675. https://doi.org/10.1016/j.eswa.2011.02.133

[13] Lee, J., Go, H., Lee, H., Cho, S., Sung, M., Kim, J. (2021). Ctrl-C: Camera calibration transformer with line-classification. In Proceedings of the IEEE/CVF International Conference on Computer Vision, Montreal, QC, Canada, pp. 16228-16237. https://doi.org/10.1109/ICCV48922.2021.01592

[14] Nguyen, T., Chen, S.W., Shivakumar, S.S., Taylor, C.J., Kumar, V. (2018). Unsupervised deep homography: A fast and robust homography estimation model. IEEE Robotics and Automation Letters, 3(3): 2346-2353. https://doi.org/10.1109/LRA.2018.2809549

[15] Wang, C., Wang, X., Bai, X., Liu, Y., Zhou, J. (2019). Self-supervised deep homography estimation with invertibility constraints. Pattern Recognition Letters, 128: 355-360. https://doi.org/10.1016/j.patrec.2019.09.021

[16] Fang, J., Vasiljevic, I., Guizilini, V., Ambrus, R., Shakhnarovich, G., Gaidon, A., Walter, M.R. (2022). Self-supervised camera self-calibration from video. In 2022 International Conference on Robotics and Automation (ICRA), Philadelphia, PA, USA, pp. 8468-8475. https://doi.org/10.1109/ICRA46639.2022.9811784

[17] Lee, J., Sung, M., Lee, H., Kim, J. (2020). Neural geometric parser for single image camera calibration. In European Conference on Computer Vision, pp. 541-557. https://doi.org/10.1007/978-3-030-58610-2_32

[18] Schaffalitzky, F., Zisserman, A. (2000). Planar grouping for automatic detection of vanishing lines and points. Image and Vision Computing, 18(9): 647-658. https://doi.org/10.1016/S0262-8856(99)00069-4

[19] Le, H., Liu, F., Zhang, S., Agarwala, A. (2020). Deep

homography estimation for dynamic scenes. In Proceedings of the IEEE/CVF Conference on Computer Vision and Pattern Recognition, pp. 7652-7661. https://openaccess.thecvf.com/content_CVPR_2020/papers/Le_Deep_Homography_Estimation_for_Dynamic_Scenes_CVPR_2020_paper.pdf.

[20] Yu, J., Liu, Y., Zhang, Z., Gao, F., Gao, N., Meng, Z., Jiang, X. (2022). High-accuracy camera calibration method based on coded concentric ring center extraction. Optics Express, 30(23): 42454-42469. https://doi.org/10.1364/OE.470990

[21] Su, Y., Guo, X., Shen, Y. (2024). Camera self-calibration from two views with a common direction. Proceedings Copyright, 680: 685. https://doi.org/10.5220/0012438100003660

[22] Zhang, B., Zhang, Z., Gu, X. (2025). A novel closed-form solution for automatic calibration of extrinsic parameters based on plane-induced homography. Robotics and Autonomous Systems, 194: 105144. https://doi.org/10.1016/j.robot.2025.105144

[23] Ngoc, V.N., Van, C.D. (2024). Development of an automatic measurement and classification system for a robotic arm using machine vision. International Journal of Mechanical Engineering and Robotics Research, 13(4): 489-494. https://doi.org/10.18178/ijmerr.13.4.489-494

[24] Wang, C., Ding, Y., Cui, K., Li, J., Xu, Q., Mei, J. (2025). A perspective distortion correction method for planar imaging based on homography mapping. Sensors, 25(6): 1891. https://doi.org/10.3390/s25061891

[25] Genovese, K. (2024). Single-image camera calibration with model-free distortion correction. Optics and Lasers in Engineering, 181: 108348. https://doi.org/10.1016/j.optlaseng.2024.108348